Effects of finite and discrete sampling and blur on microrheology experiments

VICTORIA E. LOOSEMORE AND NANCY R. FORDE*

Simon Fraser University, Department of Physics, 8888 University Dr, Burnaby, BC, V5A 1S6, Canada
*nforde@sfu.ca

Abstract: The frequency-dependent viscous and elastic properties of fluids can be determined from measurements of the thermal fluctuations of a micron-sized particle trapped by optical tweezers. Finite bandwidth and other instrument limitations lead to systematic errors in measurement of the fluctuations. In this work, we numerically represented power spectra of bead position measurements as if collected by two different measurement devices: a quadrant photodiode, which measures the deflection of the trapping laser; and a high-speed camera, which images the trapped bead directly. We explored the effects of aliasing, camera blur, sampling frequency, and measurement time. By comparing the power spectrum, complex response function, and the complex shear modulus with the ideal values, we found that the viscous and elastic properties inferred from the data are affected by the instrument limitations of each device. We discuss how these systematic effects might affect experimental results from microrheology measurements and suggest approaches to reduce discrepancies.

OCIS codes: (350.4855) Optical tweezers or optical manipulation; (120.0120) Instrumentation, measurement, and metrology.

References and links

1. B. D. Hoffman and J. C. Crocker, "Cell mechanics: dissecting the physical responses of cells to force," Annu. Rev. Biomed. Eng. **11**, 259–288 (2009).
2. D. Wirtz, "Particle-tracking microrheology of living cells: principles and applications," Annu. Rev. Biophys. **38**, 301–26 (2009).
3. T. A. Waigh, "Microrheology of complex fluids," Rep. Prog. Phys. **68**, 685–742 (2005).
4. T. A. Waigh, "Advances in the microrheology of complex fluids," Rep. Prog. Phys. **79**, 074601 (2016).
5. I. Y. Wong, M. L. Gardel, D. R. Reichman, E. R. Weeks, M. T. Valentine, A. R. Bausch, and D. A. Weitz, "Anomalous diffusion probes microstructure dynamics of entangled F-actin networks," Phys. Rev. Lett. **92**, 178 101 (2004).
6. T. G. Mason, K. Ganesan, J. van Zanten, D. Wirtz, and S. Kuo, "Particle Tracking Microrheology of Complex Fluids," Phys. Rev. Lett. **79**, 3282–3285 (1997).
7. T. G. Mason, H. Gang, and D. A. Weitz, "Diffusing-wave-spectroscopy measurements of viscoelasticity of complex fluids," J. Opt. Soc. Am. **14**, 139 (1997).
8. R. E. Mahaffy, C. K. Shih, F. C. MacKintosh, and J. Käs, "Scanning probe-based frequency-dependent microrheology of polymer gels and biological cells," Phys. Rev. Lett. **85**, 880–883 (2000).
9. A. R. Bausch, W. Möller, and E. Sackmann, "Measurement of local viscoelasticity and forces in living cells by magnetic tweezers," Biophys. J. **76**, 573–579 (1999).
10. B. Schnurr, F. Gittes, F. C. Mackintosh, and C. F. Schmidt, "Determining Microscopic Viscoelasticity in Flexible and Semiflexible Polymer Networks from Thermal Fluctuations," Macromolecules **9297**, 7781–7792 (1997).
11. K. M. Addas, C. F. Schmidt, and J. X. Tang, "Microrheology of solutions of semiflexible biopolymer filaments using laser tweezers interferometry," Phys. Rev. E **70**, 1–16 (2004).
12. D. Mizuno, D. A. Head, F. C. MacKintosh, and C. F. Schmidt, "Active and Passive Microrheology in Equilibrium and Nonequilibrium Systems," Macromolecules **41**, 7194–7202 (2008).
13. R. R. Brau, J. M. Ferrer, H. Lee, C. E. Castro, B. K. Tam, P. B. Tarsa, P. Matsudaira, M. C. Boyce, R. D. Kamm, and M. J. Lang, "Passive and active microrheology with optical tweezers," J. Opt. **9**, S103–S112 (2007).
14. H. Lee, Y. Shin, S. T. Kim, E. L. Reinherz, and M. J. Lang, "Stochastic optical active rheology," Appl. Phys. Lett. **101**, 1–4 (2012).
15. A. van der Horst and N. R. Forde, "Calibration of dynamic holographic optical tweezers for force measurements on biomaterials," Opt. Express **16**, 20 987 (2008).
16. T. Savin and P. S. Doyle, "Static and Dynamic Errors in Particle Tracking Microrheology," Biophys. J. **88**, 623–638 (2005).

17. T. Savin and P. S. Doyle, "Role of a finite exposure time on measuring an elastic modulus using microrheology," Phys. Rev. E **71**, 6–11 (2005).
18. W. P. Wong and K. Halvorsen, "The effect of integration time on fluctuation measurements: calibrating an optical trap in the presence of motion blur," Opt. Express **14**, 12 517–31 (2006).
19. A. van der Horst and N. R. Forde, "Power spectral analysis for optical trap stiffness calibration from high-speed camera position detection with limited bandwidth." Opt. Express **18**, 7670–7677 (2010).
20. K. Berg-Sørensen and H. Flyvbjerg, "Power spectrum analysis for optical tweezers," Rev. Sci. Instrum. **75**, 594–612 (2004).
21. W. W. Graessley, *Polymeric Liquids and Networks: Dynamics and Rheology* (Taylor & Francis Group, LLC, 2008).
22. J. Y. Huh and E. M. Furst, "Colloid dynamics in semiflexible polymer solutions," Phys. Rev. E **74** (2006).
23. M. Shayegan and N. R. Forde, "Microrheological characterization of collagen systems: from molecular solutions to fibrillar gels," PLoS ONE **8**, 23–28 (2013).
24. M. Shayegan, T. Altindal, E. Kiefl, and N. R. Forde, "Intact Telopeptides Enhance Interactions between Collagens," Biophys. J. **111**, 2404–2416 (2016).
25. A. D. Wessel, M. Gumalla, J. Grosshans, and C. F. Schmidt, "The mechanical properties of early drosophila embryos measured by high-speed video microrheology," Biophys. J. **108**, 1899–1907 (2015).
26. S. F. Nørrelykke and H. Flyvbjerg, "Harmonic oscillator in heat bath: Exact simulation of time-lapse-recorded data and exact analytical benchmark statistics," Phys. Rev. E **83**, 1–10 (2011).
27. K. Ohta and H. Ishida, "Comparison among several numerical integration methods for Kramers-Kronig transformation," Appl. Spectrosc. **42**, 952–957 (1988).
28. D. S. Martin, M. B. Forstner, and J. A. Käs, "Apparent Subdiffusion Inherent to Single Particle Tracking," Biophys. J. **83**, 2109–2117 (2002).

1. Introduction

Microrheology is an approach for understanding how complex fluids (fluids which exhibit both viscous and elastic properties) respond to stress or deformation on the micrometer scale. It is particularly relevant in the biological sciences where viscoelasticity is integral to the functions of cells, whose mechanical properties are essential for mechanisms such as cell growth, stem-cell differentiation, cell crawling, wound healing, protein regulation, cell malignancy, and even cell death [1, 2].

Many different techniques have been developed for microrheology [3, 4]. The predominant techniques include particle tracking, which examines particles' thermal diffusion trajectories while immersed in a viscoelastic medium [5, 6]; diffusing-wave spectroscopy, which analyses the time dependence of the light scattered from a collection of colloidal probe particles embedded in a semi-transparent viscoelastic material [7]; atomic force microscopy, where a microscopic bead is attached to a cantilever and oscillated above the surface of medium [8]; magnetic tweezers, where particles are manipulated in the medium of interest using a magnetic field [9]; and optical tweezers, where particles are trapped using a laser beam [3, 10–12], as shown schematically in the Fig. 1 inset.

Optical tweezers can be used for both active and passive microrheology [12–14]. Optical tweezers offer the additional advantage of being able to manipulate independently the positions of multiple particles within a sample simultaneously [15]. However, the simultaneous detection of more than two particle positions requires the use of camera imaging, in which effects such as finite exposure time and bandwidth can have a substantial impact on the inferred dynamics of the particles [16–19].

In this paper, we consider optical tweezers used to confine and measure the thermal fluctuations of a micron-sized particle, employing the passive approach to microrheology. Analysis of the motion of the bead gives the complex shear modulus, i.e. the viscous and elastic properties, of the fluid in which the bead is immersed [10].

The position of an optically trapped bead can be measured by imaging with a camera or by detecting the bead-induced laser deflection (of either the trapping laser or a separate detection laser). The latter generally uses a quadrant photodiode (QPD), which has a high bandwidth: 100 kHz or more. Camera imaging has lower bandwidth, with even high-speed cameras having acquisition rates of just a few kHz. Both methods sample at discrete times and can experience

aliasing. This results in signal above the Nyquist frequency (defined as half the sampling frequency: $f_{\text{Nyq}} = 1/2 \times f_s$) contributing to the measured signal at lower frequencies [20]. Measurements of position from a high-speed camera also suffer from blur due to the finite exposure time.

Due to limited bandwidth, aliasing, and blur, the sampled signals from detectors will not match the expected, infinite-bandwidth results. In this work, we aimed to determine how these parameters impact the extracted elastic and viscous moduli of a system. For simplicity, we examined a model system of a bead trapped in water, in which both the elasticity (from the trap) and viscosity (from the water) are frequency-independent. We assumed the positions of the bead were measured at discrete times with either a high-speed camera (with blur and potential aliasing) or via the deflection of a laser beam on a QPD (with potential aliasing). From the expected position power spectrum acquired by each device, we determined numerically the complex shear modulus. By comparing the results with those expected for a bead trapped in water, we assess the effects of blur, aliasing and finite sampling.

In the next section, we describe the method of obtaining the complex shear modulus from the positions of a trapped bead. We also discuss modifications required for describing the effects of aliasing and blur. These descriptions will be necessary for numerically representing potential experimental results, which is described in the Results and Discussion section. Finally, based on our results, we provide some experimental context in the Experimental Implications section.

2. Theory: from position measurements to the complex shear modulus

The complex shear modulus can be used to describe the viscous and elastic properties of fluids. It is expressed in terms of its real and imaginary parts, the elastic modulus and the viscous modulus, respectively, as [21]

$$G^*(f) = G'(f) + iG''(f). \tag{1}$$

Initially, we disregard the effects of sampling from high-speed cameras or QPDs, and follow the method proposed by Schmidt and colleagues [10] to find $G'(f)$ and $G''(f)$ for a complex fluid using optical tweezers.

First, the positions of the trapped bead, $x(t)$, are Fourier transformed to give the power spectral density (PSD) of the bead's position.

$$S(f) = \frac{2|\tilde{x}(f)|^2}{T_{\text{msr}}}, \tag{2}$$

where $\tilde{x}(f)$ is the Fourier transform of the particle's position, $x(t)$, and T_{msr} is the measurement time.

From the PSD, the fluctuation-dissipation theorem can be used to relate the magnitude of the fluctuating force to the energy dissipation, $k_B T$. This dissipation relates to the power spectrum of a particle's displacement (fluctuations) by

$$A''(f) = \frac{\pi f}{2k_B T} \times S(f), \tag{3}$$

where A'' is the imaginary part of the complex response function. Then a Kramers-Kronig relation is used to determine the real part of the sample's complex response to fluctuations, giving

$$A'(f) = \frac{2}{\pi} \text{P} \int_0^\infty \frac{\xi A''(\xi)}{(\xi^2 - f^2)} d\xi, \tag{4}$$

where P denotes the Cauchy principal value. $A'(f)$ and $A''(f)$ connect the Fourier transform of the particle's displacement, $\tilde{x}(f)$, to the Fourier transform of the force, $\tilde{F}(f)$, as $\tilde{x}(f) = A^*(f) \cdot \tilde{F}(f)$, where $A^*(f) = A'(f) + iA''(f)$.

Finally the complex shear modulus can be calculated via the generalized Stokes-Einstein relation to give

$$G^*(f) = \frac{1}{6\pi R A^*(f)}. \tag{5}$$

R is the radius of the probe particle. Through this definition, G'' should be negative but, by convention, its magnitude will be taken. Both A' and A'' contribute (unequally) to G' and G'' as

$$G'(f) = \frac{1}{6\pi R} \left(\frac{A'}{A'^2 + A''^2} \right) \tag{6}$$

$$G''(f) = \frac{1}{6\pi R} \left(\frac{A''}{A'^2 + A''^2} \right). \tag{7}$$

These steps have been applied to determine the complex shear modulus of many systems, including actin networks, collagen solutions and networks, cellulose, other polymer networks, and even live embryos [11–13, 22–25]

2.1. Ideal behaviour of a trapped bead in water

For water, a purely viscous fluid, the theoretical power spectral density of the bead's position takes the shape of a Lorentzian function,

$$S(f) = \frac{D}{\pi^2} \times \frac{1}{(f^2 + f_c^2)}, \tag{8}$$

where D is the diffusion constant (a function of the bead radius, viscosity of the fluid, and system temperature), and f_c is called the corner frequency, which is related to the trap stiffness. At frequencies below the corner frequency, the bead is constrained by the trap; at frequencies above f_c, the bead is freely diffusing within the trap. This treatment disregards inertial effects, which contribute at frequencies above ~1 MHz (depending on bead size) [20]. Calculations using the Lorentzian form of the power spectral density will be referred to as the ideal, infinite-bandwidth results.

From this PSD, Eqs. (3) and (4) can be used directly to obtain the complex response function. The results are

$$A''(f) = \frac{Df}{2\pi k_B T(f^2 + f_c^2)}, \tag{9}$$

and

$$A'(f) = \frac{Df_c}{2\pi k_B T(f^2 + f_c^2)}. \tag{10}$$

For a purely viscous fluid like water, the measured elastic modulus, $G'(f)$ arises only from the stiffness of the optical trap and is independent of frequency:

$$G'(f) = \frac{\kappa}{6\pi R}, \tag{11}$$

where R is the radius of the trapped bead and κ is the trap stiffness ($\kappa = 12\pi^2 \eta R f_c$). The dynamic viscosity of water, η, is similarly independent of frequency, and thus the viscous modulus behaves as

$$G''(f) = 2\pi \eta f. \tag{12}$$

Therefore, when the viscous modulus and frequency are plotted on logarithmic scales, a linear relation with a slope of 1 is expected, with a value of $G''(f) = \log(2\pi\eta)$ at $f = 1$ Hz, henceforth called the intercept.

2.2. Accounting for aliasing and blur

By including aforementioned issues with finite and discrete sampling, the Lorentzian form of the PSD is altered within the detected frequency range. For the QPD, the limited bandwidth induces aliasing which changes the shape of the PSD. Therefore the power spectrum associated with a trapped bead in water can no longer be defined as a simple Lorentzian, as in Eq. (8), but must also include the aliased frequencies. For a single-sided spectrum one expects

$$S(f) = \sum_{n=-\infty}^{\infty} \frac{D}{\pi^2((2nf_{\mathrm{Nyq}} + f)^2 + f_c^2)}, \tag{13}$$

which has a similar form to the double-sided treatment in [19]. For bead positions sampled at N discrete times, with $\Delta t = 1/f_s$, the explicit form of the aliased single-sided PSD is [26],

$$S(f) = \frac{D(1 - c^2)\Delta t}{\pi f_c(1 + c^2 - 2c\cos(2\pi f/N))}, \tag{14}$$

where $c = \exp(-2\pi f_c \Delta t)$.

For the high-speed camera, the power spectral density of the bead's position includes aliasing and also blur [19]. It takes the form

$$S(f) = \sum_{n=-\infty}^{\infty} \frac{D}{\pi^2((2nf_{\mathrm{Nyq}} + f)^2 + f_c^2)} \left(\frac{\sin\left(W\pi \left|2nf_{\mathrm{Nyq}} + f\right|\right)}{W\pi \left|2nf_{\mathrm{Nyq}} + f\right|} \right)^2, \tag{15}$$

where W is the integration time.

For both high-speed camera and QPD position measurements, there will be a position detection error in experiments. However, for the purposes of the current study, these errors are omitted from the calculations. The effects of particle-tracking errors on power spectral calibration [19] and on microrheology measurements [16] have previously been considered by others .

3. Results and discussion

In order to numerically calculate the experimentally-expected complex shear modulus, we first calculated the PSD at frequency intervals of $\Delta f = 1$ Hz. This corresponds to a measurement time $T_{\mathrm{msr}} = 1$ s. Calculations were performed for a bead trapped in water (viscosity $\eta = 9.58 \times 10^{-4}$ Pa·s), with a system temperature of $T = 295$ K, a bead radius of $R = 1$ μm, and a corner frequency of $f_c = 100$ Hz, which corresponds to a trap stiffness $\kappa = 1.13 \times 10^{-5}$ N/m [20]. $G'(f)$ and $G''(f)$, calculated as described in the previous section, will be compared to the expected values. The sampling frequency for the QPD-like data was set to $f_s = 100$ kHz and the high-speed camera-like sampling frequency was $f_s = 2500$ Hz. Additionally, the camera-like data include the effects of blur. Blur is related to the sampling frequency; here, we assumed simply that $W = f_s^{-1} = 4.0 \times 10^{-4}$ s.

Figure 1 shows the infinite-bandwidth power spectrum of a trapped bead's position in water (Eq. (8)), the QPD-like PSD (Eq. (13)) and the camera-like PSD (Eq. (15)) over their experimentally relevant frequency ranges. Note that Eqs. (13) and 15 have summations from $n = -\infty$ to ∞ to include all aliased frequencies. In the calculations performed here, the summation was limited to $n = -2$ to 2. Since the Lorentzian function continues to decrease with increased frequency, the errors introduced by neglecting these values should be minimal. The validity of this approach will be discussed later.

As expected, the only discrepancy observed among 'device-like' and continuous Lorentzian PSDs is at high frequencies, wherein the contributions of finite sampling, aliasing, and blur become apparent. The camera-like data, cut off at $f_{\mathrm{Nyq}} = 1250$ Hz, experience a curl-up due
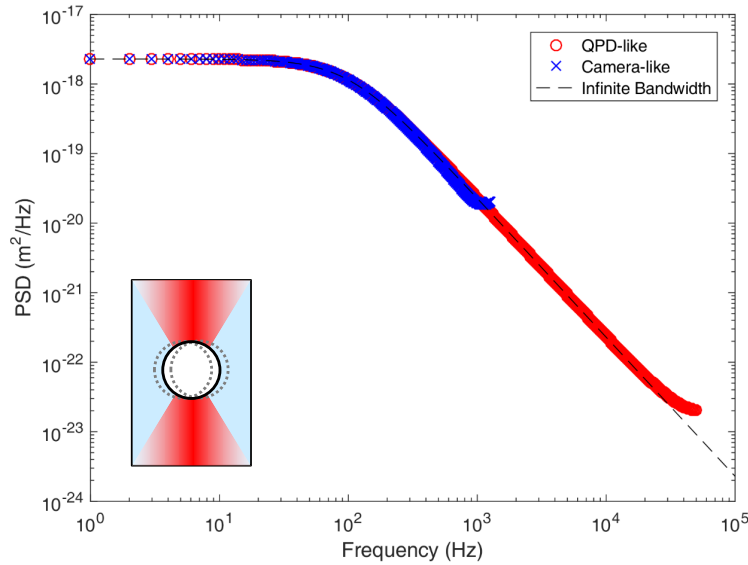
Fig. 1. The calculated power spectral densities (PSD) of the constrained motion of a trapped bead in water (inset) with radius $R = 1$ μm, temperature $T = 295$ K, and corner frequency $f_c = 100$ Hz. The PSDs for QPD-like measurements (red circles) and for camera-like measurements (blue x's) are compared with the continuous Lorentzian result (black, dashed).

to blur and aliasing; the QPD-like data show a flattening due to aliasing while being cut off at $f_{\text{Nyq}} = 50$ kHz.

The high-frequency distortions in the PSD propagate to high frequencies in $A''(f)$ (Eq. (3)), as shown in Fig. 2(b). $A''(f)$ is plotted for the QPD-like, camera-like, and ideal data, with ratios of device-like to ideal results plotted in the upper figure. The QPD-like data deviate above the ideal values at frequencies higher than 500 Hz, while the camera-like data decreases below ideal values beyond 100 Hz.

The effects of finite sampling become more pronounced in calculating $A'(f)$ (Eq. (4)). In Fig. 2(a), the QPD-like, camera-like and ideal data are plotted, with the ratios of device-like to ideal, infinite-bandwidth data shown in the top plot. The camera-like $A'(f)$ underestimates the ideal values at all frequencies. For both QPD-like and camera-like data, $A'(f)$ drops off at high frequencies. This is because of the Kramers-Kronig relation, which requires integration to infinite frequency. With discrete sampling and data limited by the Nyquist frequency, the integral in Eq. (4) can only be approximated by

$$A' \approx \frac{2}{\pi} \text{P} \int_{\Delta f}^{f_{\text{Nyq}}} \frac{\xi A''(\xi)}{(\xi^2 - f^2)} d\xi \tag{16}$$

which can be numerically determined with the trapezoidal approximation

$$\int_a^b f(x)dx \approx \frac{b-a}{2N} \sum_{n=1}^{N} (f(x_n) + f(x_{n+1})). \tag{17}$$

This results in distortions in $A'(f)$ over a wide range of high frequencies as well as at low frequencies, where QPD-like values of $A'(f)$ are also underestimated (Fig. 2(a)).
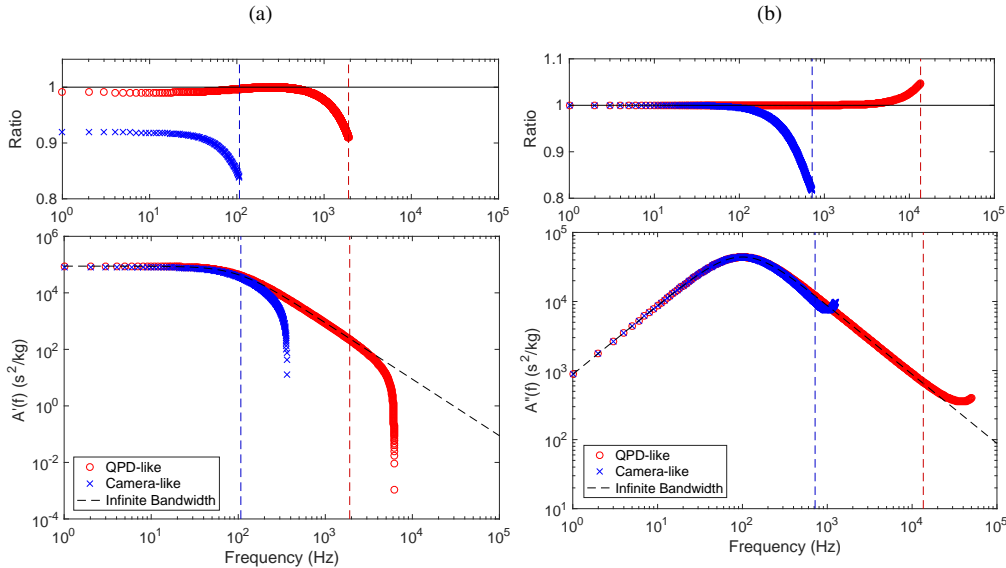
Fig. 2. Lower: (a) $A'(f)$ and (b) $A''(f)$ for the ideal, infinite-bandwidth treatment (black, dashed), QPD-like data (red circles), and high-speed camera-like data (blue x's). Upper: Ratios of device-like values to the ideal values. At low frequencies, there is a discrepancy only in $A'(f)$, while both $A'(f)$ and $A''(f)$ differ from the ideal predictions at high frequencies. Vertical dashed lines correspond to cut-off frequencies determined from $G^*(f)$ data; see text for details.

From $A^*(f)$, the complex shear modulus is calculated using Eqs. (6) and (7). Figure 3 shows the calculated $G'(f)$ and $G''(f)$ for the device-like and ideal data. The ratios of device-like to ideal values are shown above. These ratios are cut off at frequencies where the data drops off significantly (by $\geq 10\%$) from the expected trend. For $G'(f)$, this cut-off frequency is defined by a deviation from the expected plateau, i.e., $G'(f_{cut-off}) \leq 0.9G'(f)_{max}$. For $G''(f)$, the cut-off frequency is defined by the deviation of the slope of $\log(G''(f))$ vs $\log(f)$ from the expected value of 1, i.e., slope ≥ 1.1 or ≤ 0.9. These cut-off points are shown as red and blue dashed lines for the QPD-like and camera-like data, respectively. Large underestimates are expected at high frequencies due to the aforementioned approximation of the $A'(f)$ integration (Eq. (16)) [27].

The values of viscosity, η, and G'_{trap} are calculated from $G''(f)$ and $G'(f)$ only below their respective cut-off frequencies. To obtain η, $\log(G''(f))$ vs $\log(f)$ is fit with a line of slope $= 1$, and the intercept (at $f = 1$ Hz) gives the viscosity. The QPD-like data report a value of $\eta_{QPD} = 9.31 \times 10^{-4}$ Pa·s while the camera-like data report $\eta_{cam} = 1.09 \times 10^{-3}$ Pa·s. Compared to the input (and ideal output) value of $\eta_{ideal} = 9.58 \times 10^{-4}$ Pa·s, the QPD-like data underestimate the true value by 3% while the camera-like data overestimate it by 12%. It is obvious from the ratio plot of $G''(f)$ (Fig. 3(b), top) that the camera-like $G''(f)$ values exceed the ideal values at all frequencies below the cut-off frequency, consistent with the overestimation of η. The underestimate of η from the QPD data likely arises because many high-frequency data points are included in the fit that are smaller than the expected values. The estimate of η from the QPD $G''(f)$ values can be improved by a more stringent selection of the cut-off frequency (data not shown).

Similarly, for $G'(f)$, the QPD-like data underestimate the infinite-bandwidth plateau of
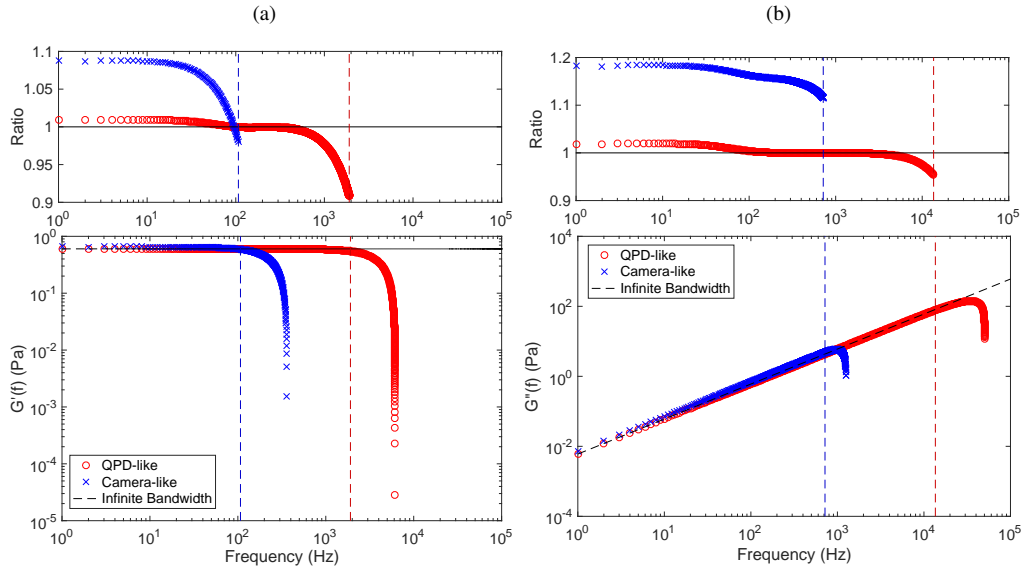
Fig. 3. Lower: Calculated (a) elastic and (b) viscous modulus for the ideal, infinite bandwidth case (black, dashed), QPD-like data (red circles) and camera-like data (blue x's) for values corresponding to experimental data in Figs. 1 and 2. Upper: Ratios of device-like data to ideal (a) $G'(f)$ and (b) $G''(f)$, displayed up to the relevant cut-off frequencies. At high frequencies, there is a drop-off in device-like values, related to the finite sampling. At low frequencies, device-like values overestimate the moduli. Red and blue dashed lines show the cut-off frequencies for the QPD-like and camera-like data, as described in the text.

G'_{ideal} = 0.602 Pa with G'_{QPD} = 0.585 Pa and the camera-like data overestimate it with G'_{cam} = 0.631 Pa. These values were determined by fitting a zero-slope line to the $G'(f)$ data up to the cut-off frequency. The ratio plot of $G'(f)$ in Fig. 3 shows the camera-like data above the ideal values, while the QPD-like data have many points below the ideal plateau at high frequencies.

To differentiate between the effects of blur and aliasing in the camera-like data, the sampling frequency of the QPD-like data was reduced to f_s = 2500 Hz. Results are presented in Fig. 4. Most notably, the added effect of blur in the camera-like data significantly worsens the estimates of both $G'(f)$ and $G''(f)$. The removal of blur at this sampling frequency of 2.5 kHz improves the estimate of η from η_{cam} = 1.09×10^{-3} Pa·s to η_{QPD} = 9.81×10^{-4} Pa·s, though both still overestimate the value of η_{ideal} = 9.58×10^{-4} Pa·s. The elastic modulus of the trap in the absence of blur, G'_{QPD} = 0.591 Pa, is closer to G'_{ideal} = 0.602 Pa than is the estimate with blur, G'_{cam} = 0.631 Pa. The underestimation by G'_{QPD} again results from the choice of cut-off frequency.

Markedly, all of these analyses have found an overestimation of $G'(f)$ and $G''(f)$ at low frequencies. This finding is reiterated at other corner frequencies (data not shown). A discrepancy at low frequencies first appears in $A'(f)$ (Fig. 2(a)). Since $A'(f)$ results from a Kramers-Kronig relation, the low frequency discrepancy in $G'(f)$ and $G''(f)$ may result from the numerical approximations used in this integration (Eqs. (16) and (17)).

To demonstrate how finite sampling contributes to the response at low frequency, we calculated
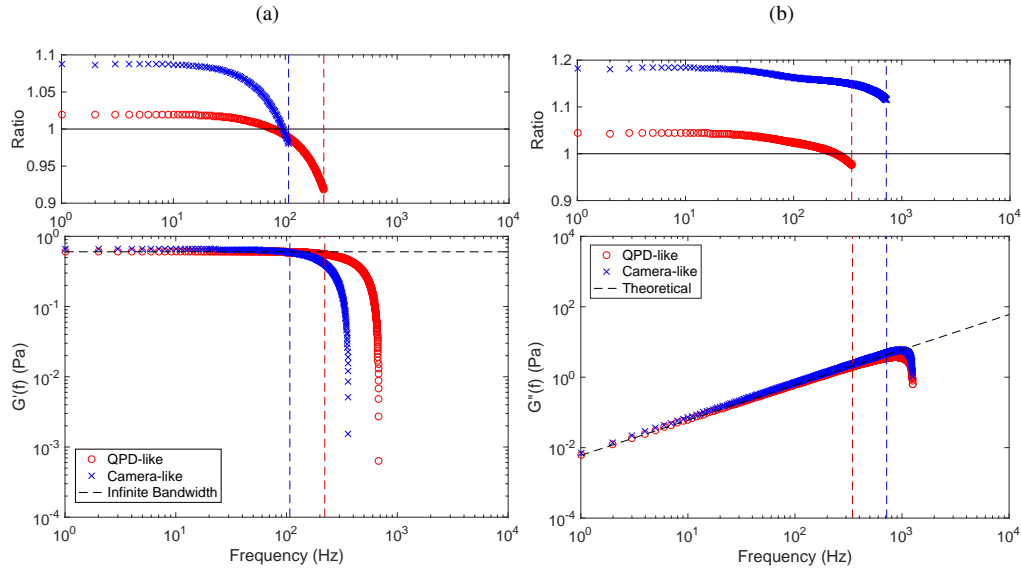
Fig. 4. The (a) elastic and (b) viscous moduli for the ideal, infinite-bandwidth case (black, dashed), QPD-like data sampled at f_s = 2500 Hz (red circles), and camera-like data (blue x's), with ratio plots. The blur associated with the camera-like data worsens the estimate of the $G'(f)$ plateau (trap stiffness) and the $G''(f)$ intercept (viscosity). Red and blue dashed lines show the cut-off frequencies for the QPD-like and camera-like data, respectively, which are altered by the effect of blur.

the PSD instead with a frequency interval Δf = 0.1 Hz, corresponding to T_{msr} = 10 s. Figure 5 shows a comparison of $G'(f)$ and $G''(f)$ from QPD-like data (with ratio plots) previously calculated at 1 Hz increments with Δf = 0.1 Hz.

As is evident from the ratio plots of Fig. 5, the Δf = 0.1 Hz data provide a better estimate of the true value of the complex shear modulus at low frequencies than does Δf = 1 Hz., while leaving the cut-off frequencies essentially unaltered. Although the extracted values of G'_{trap} and η are changed very little (G' = 0.582 Pa and η = 9.32×10^{-4} Pa·s for Δf = 0.1 Hz), it is clear that the values of $G'(f)$ and $G''(f)$ at low frequency are better represented in this data set.

Similar results are shown in Fig. 6, where $G'(f)$ and $G''(f)$ of the camera-like data are shown for both Δf = 1 Hz and Δf = 0.1 Hz. In this case also, the low-frequency values of the moduli approach closer to the ideal, infinite-bandwidth expectations. However, due to the effects of blur, the ratios do not approach as closely to 1 as the QPD-like data do. For Δf_{cam} = 0.1 Hz, G' = 0.627 Pa and η = 1.08×10^{-3} Pa·s, representing a small but systematic improvement.

Since the Δf = 0.1 Hz data provide a better estimate of the true complex shear modulus values, the low-frequency underestimation of the principal value in determining $A'(f)$ (leading to an overestimation of $G'(f)$ and $G''(f)$) can be attributed to the discrete sampling of the device-like data. In calculating the integral in Eq. (16), there is a pole at ξ = f, which makes the integration challenging. As mentioned, the integration was accomplished using the trapezoidal method [27], and omitting the pole. This results in an underestimation of the value of the integral. By including data points closer to the pole, we ensure a better estimation of the principal value.

As previously mentioned, the PSDs for the QPD-like and camera-like data were calculated from summation equations 13 and 15, respectively, from n = −2 to 2. Essentially, this creates the
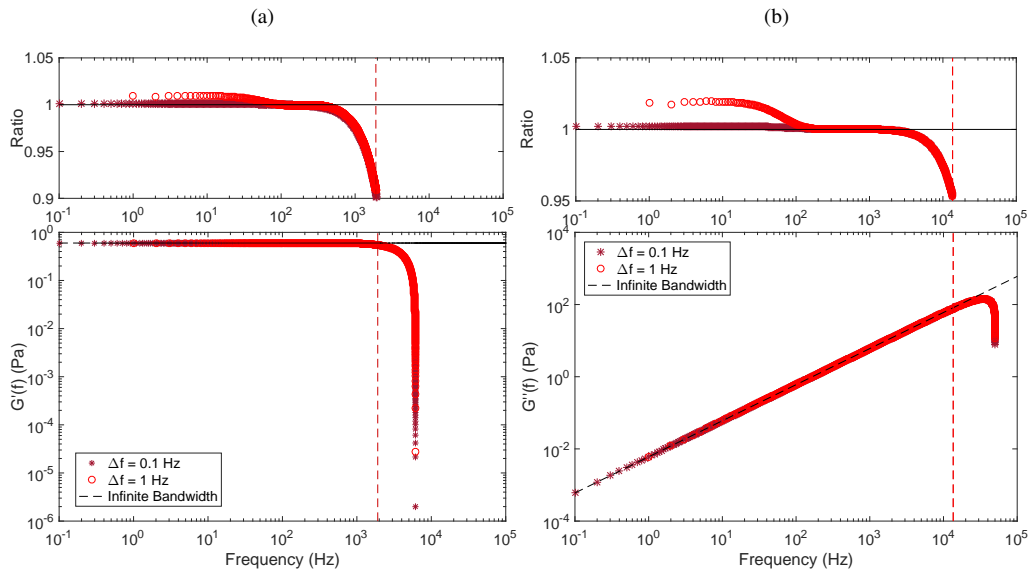
Fig. 5. The QPD-like (a) elastic and (b) viscous shear moduli for $\Delta f = 0.1$ Hz (burgundy stars) and $\Delta f = 1$ Hz (red circles), and ideal infinite-bandwidth moduli (black, dashed) with ratio plots. The cut-off frequencies are shown by red dashed lines (for both $\Delta f = 0.1$ Hz and $\Delta f = 1$ Hz).
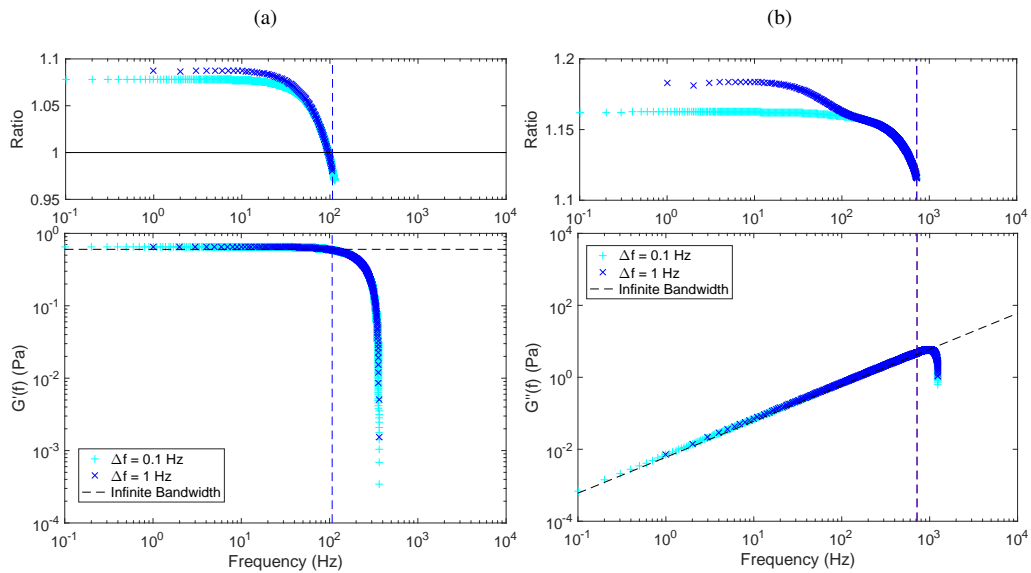

Fig. 6. The camera-like (a) elastic and (b) viscous shear moduli for $\Delta f = 0.1$ Hz (cyan +'s) and $\Delta f = 1$ Hz (blue x's), and ideal infinite-bandwidth moduli (black, dashed) with ratio plots. The cut-off frequencies are shown by blue dashed lines (for both $\Delta f = 0.1$ Hz and $\Delta f = 1$ Hz).

effect of a low-pass filter in the calculations because frequencies corresponding to $|n| > 2$ are excluded. Figure 7 compares the ideal infinite-bandwidth PSD (Eq. (8)), a perfectly anti-aliased PSD (Eq. (8) sampled discretely only from $1/T_{\text{msr}}$ to f_{Nyq}), the QPD-like definite PSD (Eq. (14)) and the summation PSD used to this point (Eq. (13) calculated from $n = -2$ to 2). The plot above shows the ratios of the PSDs from the discrete approaches to the ideal continuous prediction. As expected, both aliased forms of the PSD exhibit a flattening at high frequency. Even though $|n| \leq 2$ have been maintained in calculating the PSD from Eq. (13), there is a small but detectable difference ($\sim 10\%$) from the definite result at the highest frequencies.
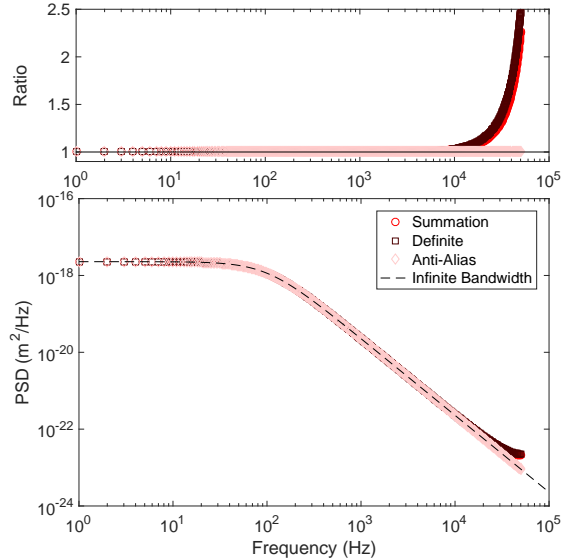

Fig. 7. Bottom: The calculated QPD-like power spectral densities using the summation method (Eq. (13); red circles), the definite method (Eq. (14); burgundy squares), perfectly anti-aliased data (discretely sampled Eq. (8); pink diamonds) and the infinite-bandwidth data (black dashed line). Top: Ratios of PSDs to the ideal infinite-bandwidth PSD.

The treatment of aliasing has a significant effect on the extracted values of the complex shear modulus, particularly the elastic modulus. Figure 8 shows $G'(f)$ and $G''(f)$ resulting from the definite and summation forms of the PSD. The method using the definite equation increases the cut-off frequency of the elastic modulus by more than 400 Hz, which increases the $G'(f)$ plateau value slightly toward the infinite-bandwidth value: $G'_{\text{definite}} = 0.590$ Pa. By not including aliasing at all, the $G'(f)$ frequency range is lowered by over 100 Hz, while not affecting the plateau value ($G'_{\text{antialias}} = 0.585$ Pa). The $G''(f)$ cut-off frequency does not change as dramatically, with the anti-aliased data actually increasing the cut-off frequency. The viscosity values are changed slightly: $\eta_{\text{definite}} = 9.30 \times 10^{-4}$ Pa·s and $\eta_{\text{antialias}} = 9.34 \times 10^{-4}$ Pa·s.

This result also has implications for our previous camera-like data results, where the summation method from $n = -2$ to 2 was also used (Eq. (15)). It would therefore be expected that, if using a definite form of the PSD which included blur, the cut-off frequency for $G'(f)$ would increase, while the cut-off frequency for $G''(f)$ would decrease. However, the qualitative finding that blur significantly worsens estimates of G' and G'' (e.g. Fig. 4) is unlikely to change.

Lastly, we examined the results for a bead in water in the absence of a trap, i.e., with no elastic components and $f_c = 0$ Hz. These calculations were motivated by particle tracking experimental procedures which monitor the particles' diffusive trajectories. Figure 9(a) shows that the viscous modulus suffers at low and high frequencies due to the effects of blur, aliasing and limited
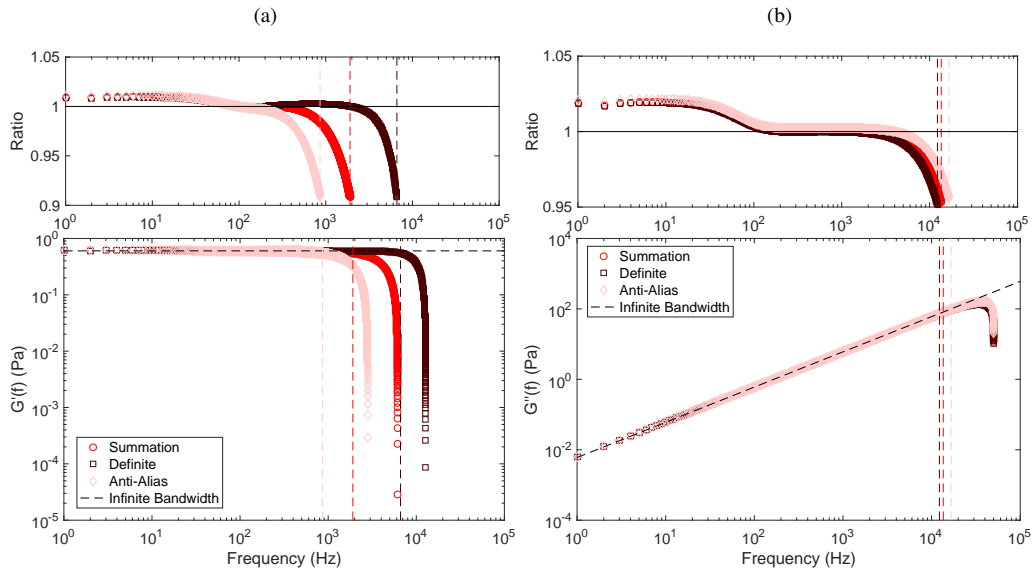
Fig. 8. Bottom: The QPD-like (a) elastic and (b) viscous shear moduli using the summation method (red circles), the definite method (burgundy squares), the anti-aliased data (pink diamonds) and the ideal infinite-bandwidth data (black, dashed). Top: Ratios of moduli to ideal infinite-bandwidth results.
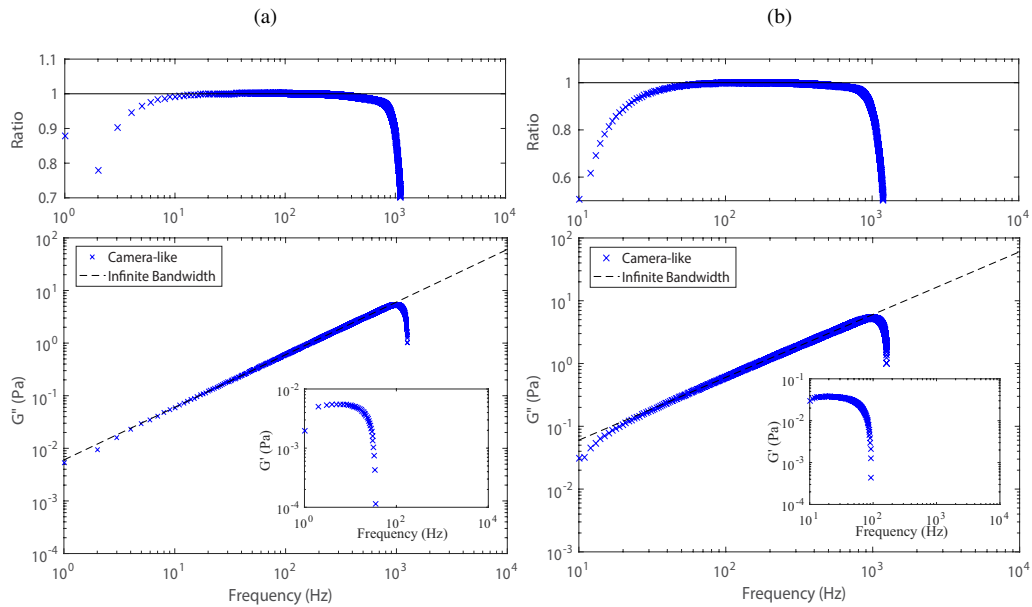

Fig. 9. Bottom: The viscous modulus for a bead in water in the absence of a trap. (a) Starting from $f = 1$ Hz and (b) starting from $f = 10$ Hz, for camera-like (blue) and infinite bandwidth (black) data. Top: Ratios of moduli to ideal infinite-bandwidth results. Insets: The elastic modulus, which is expected to be zero.

bandwidth. Additionally, these effects introduce an apparent, though small, elastic modulus in the system (Fig. 9(a) inset). To test whether this apparent elasticity arises from a lack of information about the system's response at low frequencies, we eliminated the first few data points in the power spectrum, such that information started at $f = 10$ Hz. This results in a worsened overestimate of G', while altering estimates of G'' most at its lowest frequencies (Fig. 9(b)).

4. Experimental implications

We have shown that blur arising from the finite exposure time of a high-speed camera will cause an overestimation of $G'(f)$ and $G''(f)$. Similar effects of blur have been documented for other model fluid systems [17]. For the values considered in this work, the overestimate of modulus can be as high as 20%. For experimental work, it would be advisable to reduce the exposure time and hence blur, although, sufficient light levels are needed to minimize particle tracking error. Particle tracking error, not considered in this study, has previously been shown to introduce artefacts into microrheology data, which may in some cases act to apparently compensate for the overestimate of elasticity arising from blur [16, 28].

Finite, discrete sampling has other effects on the extracted complex shear modulus. Notably, the Kramers-Kronig relation requires continuous, infinite data series, which are experimentally impossible. We have shown that it is possible to improve estimates from this relation by having data at smaller intervals in frequency. To achieve this experimentally one could sample for longer times (since $\Delta f = 1/T_{\mathrm{msr}}$), which would result in smaller frequency intervals in the PSD. However, this can be impractical due to drift or the desire to measure the time-dependent evolution of viscoelasticity of a dynamical system. Instead, we suggest interpolating between experimental data points in the power spectrum. This method doesn't add new information: it simply increases the density of values in frequency space, which means that points closer to the poles in the integration (Eq. (16)) are included and leads to improved low-frequency estimates of $G'(f)$ and $G''(f)$. This method assumes that the complex modulus is smooth over the originally-sampled frequency interval (e.g. $\Delta f = 1$Hz), a valid approximation for systems studied using this technique. Alternative approaches to solving the Kramers-Kronig relation may be implemented [10], though these may not perform as well as the integration method used here [27].

We have also shown that the frequency range contributing to the measurements affects the output results. The use of a perfect anti-aliasing filter (low-pass filter at f_{Nyq}) results in a considerably shorter range of frequencies over which both G'_{trap} and η can be considered constant. Increasing the cut-off frequency of this low-pass filter (to include higher-order contributions from aliasing) increases the frequency range of expected response by as much as an order of magnitude for G' for the values considered here (Fig. 8). This result implies that using an anti-aliasing filter in microrheological measurements will limit the frequency range over which the response can be measured, far below the cut-off frequency of the filter itself.

Additionally, we presented calculations representing a system with no optical trap, motivated by understanding sampling effects on particle tracking experiments using a high-speed camera. Our results show that care must be taken when analysing these data. The viscous modulus is affected at both high and low frequencies by blur induced by the finite exposure time of the camera. Furthermore, the lack of information about particle motion below the first frequency point results, incorrectly, in the attribution of a low-frequency elastic modulus to the system. Particle tracking error would certainly also contribute substantially to such experimental measurements, as beads diffuse freely in three dimensions. While necessitating no more than a microscope equipped with a high-speed camera to perform the measurements, the validation of the findings from passive particle-tracking measurements may require the use of an alternative characterization method (such as bulk rheology, optical-tweezers-based microrheology with laser-based detection, or diffusing-wave spectroscopy).

The results found in this study may lead to questions surrounding the validity of previous experimental interpretations. For experimentalists, the good news is that our numerical calculations performed mimicking the laser deflection analysis method show only small discrepancies from expected results. Thus, previous results using a quadrant photodiode or similar device to measure the fluctuations of a bead should show correct trends. However, conclusions drawn from experiments using a high-speed camera suffer from larger discrepancies due to the effects of blur. One solution to this problem would be to compare the frequency-depedent complex shear moduli from laser-based and camera-based tracking. This would reveal the range of frequencies over these measurements provide consistent results; a camera-based detection strategy could then be employed in experiments with more than two trapped particles, where laser-based bead tracking is not an easy option.

In this study, we have calculated results from a bead immersed in the simplest fluid: water, which exhibits Newtonian fluid-like properties, i.e. frequency-independent viscosity and no elasticity. However, the analysis approaches used here are also used for fluids which are non-Newtonian and exhibit both viscous and elastic behaviour and thus the findings here are cautionary to a broad range of systems.

5.   Conclusions

While microrheology using optical tweezers remains a popular tool for understanding complex fluids, the effects of finite bandwidth, aliasing, and blur brought on by the measurement instruments, as studied here, have a pronounced impact on the interpretation of the data. We numerically represented the elastic and viscous moduli including different instrument limitations. As expected, the finite bandwidth creates a drop-off for both elastic and viscous moduli at high frequencies, where the Kramers-Kronig integral, an important step in the calculation of the complex modulus, becomes underestimated. We demonstrated that blur, alone, increases the elastic and modulus at all frequencies before this drop-off. Aliasing creates only a slight effect, but significant enough to advise against using an anti-aliasing filter. We hope that the results and suggestions of this work will contribute to robust, reliable experimental analysis in the field of microrheology.

Funding